Journal of Alloys and Compounds 509 (2011) 4108–4116

Contents lists available at ScienceDirect

Journal of Alloys and Compounds

journal homepage: www.elsevier.com/locate/jallcom

Lanthanum ferrite ferromagnetic nanocrystallites by a polymeric precursor route

Monica Popa, Jose M. Calderon Moreno*

Institute of Physical Chemistry Ilie Murgulescu, Academia Romana, Splaiul Independentei 202, sector 6, Bucharest, 060021, Romania

ARTICLE INFO

Article history:
Received 28 September 2010
Received in revised form
17 December 2010
Accepted 21 December 2010
Available online 28 December 2010

Keywords:
$LaFeO_3$
Ferrites
Powders chemical preparation
Nanocrystalline powders
Magnetic properties

ABSTRACT

Reactive lanthanum orthoferrite nanoparticles were obtained by a polymeric precursor route. Nanoparticle growth and crystallization from amorphous precursor, as well as the formation of a grain boundary network in polycrystalline aggregates at different calcination temperatures were studied by conventional and high-resolution electron microscopy; electron and X-ray diffraction analysis; Raman; IR; and UV–vis spectroscopy. Microstructure measurements were compared to X-ray diffraction and chemical analysis results. Electron diffraction, combined with electron microscopy results were used to determine the content of amorphous phase. The coherent crystalline domain size and the particle size have been monitored by XRD and electron microscopy in order to determine the evolution of both crystal size and the onset temperature for crystallites formation. The results demonstrate that at 550 °C we obtain pure single-phase nanocrystalline $LaFeO_3$, sized ~40 nm, without the presence of amorphous phase. The magnetization curves in the 5–350 K range indicate weak ferromagnetism of the $LaFeO_3$ powders.

1. Introduction

Perovskite type oxides ABO_3 where position A is occupied by the rare earth ion, and position B by the transition metal ion, display significant catalytic properties making these materials of great importance to be used in advanced technologies as soft oxide fuel cells [1,2], catalysts [3,4], chemical sensors [5] and oxygen permeation membranes [6,7].

$LaFeO_3$ (LF) is a well-known ABO_3 perovskite oxide material which consists of FeO_6 octahedra units with La^{3+} ions inserted between these units. Bulk $LaFeO_3$ is known to be antiferromagnet with a Néel temperature T_N of 740 °C [8]. LF perovskite oxides are of practical interest as electro-ceramics due to their attractive mixed conductivity displaying ionic and electronic defects [9–11], due to the presence of Fe^{2+}/Fe^{3+}mixed valences, accompanied by oxygen non-stoichiometry. The mixed valence states can play a prominent role in affecting the magnetic properties of the LF materials. The great stability of the perovskite framework allows the partial substitution at the A site and/or B sites modifying the catalytic, redox and structural properties of this type of materials. Investigation of the structure is important both for basic knowledge and for applications in which materials involving electronic transfer are of interest. The structure, properties and potential applications of LF materials are strongly influenced by the synthesis processing of the precursor powders, therefore a lot of research is aimed both at its processing and characterization. The drawbacks associated to the diffusional constraints in solid state synthesis result into slow kinetics and high temperature synthesis, uncontrolled particle size and low surface area, thus generated the interest towards solution techniques involving improvement of the synthesis conditions for obtaining pure phases with the aim of lower reaction temperatures of homogeneous powders [12–20].

Based on the target applications, different synthesis methods have been used as alternative for solid state reactions and mechanical chemical solid reaction, including coprecipitation [21,22], combustion [23–26], sol–gel [27–29], gel [30] and sol–gel [31], autocombustion, polyol [32], microemulsion [33], hydrothermal [34], sonochemical [35], low temperature [36] and microwave assisted [37] thermal decomposition. However there are no studies concerning the presence of residual carbon, the calcination temperature that should be used to eliminate it, or the thermal evolution of the obtained powders: crystal size, presence of agglomerates. In this context, the synthesis of crystalline LF powders by methods that involve the use of organics, such as the amorphous complex method and the polymerizable complex method (PC method) at low temperature, based only on X-ray diffraction evidence, should not ignore the presence of residual carbon and the formation of polycrystalline agglomerates [38,39].

Within this framework, we report the synthesis and microstructure evolution of nanosized LF powders prepared from the La–Fe metal polymeric precursor by means of a simple Pechini-type polymerizable complex (PC) method based on polyesterification between citric acid and ethylene glycol [26,40]. The present research reports the crystallization process, nucleation and grain growth of LF from the amorphous precursors during thermal treatment, the amount of amorphous phases present; the crystallites

* Corresponding author.
E-mail address: jose.calderon@upc.edu (J.M.C. Moreno).

0925-8388/$ – see front matter © 2010 Elsevier B.V. All rights reserved.
doi:10.1016/j.jallcom.2010.12.162

lattice in the powders and the formation of grain boundaries and local sintering behavior above the crystallization temperature, as well as vibrational and magnetic properties of the nanocrystalline powders obtained at different temperatures. Results determine the suitability and advantages of the use of PC method to provide weak ferromagnetic homogeneous small particle size powders with high sinterability and to prepare LF ceramics at low temperatures.

2. Experimental procedures

The starting materials were $La_2O_3{\cdot}3H_2O$ and Fe-citrate (Merck). Citric acid (CA) was dissolved in water and at ~60 °C addition of lanthanum oxide and Fe citrate (1:2 molar ratio) was followed. The polymeric precursor powder preparation method has been described in detail elsewhere [26]. A clear orange solution of stable metals–citric acid complexes was obtained and ethylene glycol (EG) was added to this solution. The temperature of the solution was increased to 90 °C and kept at this temperature until the formation of a viscous and transparent lightly orange gel; as the polyesterification reaction between CA and EG occurs in the solution, the immobilization of the metal ions in the polymeric network is generated. Continuously increasing temperature determines water excess removal and also a more viscous and bubbly mass, without any precipitation. The mixture initially boils with frothing and foaming to the capacity of the container and undergoes dehydration followed by exothermic decomposition (with no flame) to yield a solid oxide product. The resulting material was treated at 400 °C and complete dehydration takes place which determines to the bottom of the container of a dark brown to black ash which was ground into a powder, referred to as the "precursor" hereafter. The colour indicates that the powder contains carbon. Based on a thermogravimetric analysis [26] the "precursor" powder was ground and heat treated in open air between 500 °C and 900 °C. The products obtained at different stages were characterized by different techniques. The colour of the powder changed with the thermal treatment temperature, from dark brown at 400 °C it became light brown to orange at 500 °C, while starting 550 °C has kept a light orange-reddish colour.

The precursor and the calcined LF powders were characterized by XRD, in a 2θ range from 15° to 75° with scanning speed of 0.75° min^{-1}, at room temperature using Cu-Kα radiation (Siemens D-500). The powder morphology was observed by scanning electron microscopy (SEM) (Zeiss EVO LS10), transmission electron microscopy (TEM) and electro-diffraction (ED) (Hitachi H800MT and JEOL 2010).

Raman spectra were measured at room temperature using a Jobin Yvon/Atago-Bussan T-64000 triple spectrometer with a liquid nitrogen cooled CCD detector. Acquisition time was between 800 s and 1200 s. The green line (λ = 514.5 nm) of Ar^+ laser was used to excite Raman spectra using a power of ~450 μW. Measurements were carried out under the microscope, using a 90× microscope objective; the laser spot size was around 1–2 μm. Raman measurements covered the range between 100 cm^{-1} and 2000 cm^{-1}.

IR spectra were obtained at a resolution of 2 cm^{-1}, over the frequency range from 1000 to 370 cm^{-1}, using a model M80 Carl Zeiss Jena Specord spectrophotometer. The spectra were taken from thin (~20 mg/cm^2) KBr pellets containing samples of approximately 1 wt.% Pellets were prepared by compacting an intimate mixture obtained by grinding 1 mg of substance in 100 mg KBr. Ultraviolet visible spectroscopy diffuse reflectance spectra were acquired with a JASCO spectrometer.

The magnetic properties of the nanocrystalline LF were studied. Measurements of the magnetization versus temperature with magnetic applied field were recorded on a home-made unit VSM (Vibrating Sample Magnetometer) with a sensitivity no less than 10^{-4} (emu/g), using Lock-in amplifier Model 5210 (USA) with temperature controller OXFORD ITC 503. Temperature variation of the magnetization was measured in the temperature range 50–350 K, at H = 500 Öe, after cooling the samples by the liquid nitrogen from room temperature down to 77 K. The magnetization curves vs. magnetic field were measured with a quantum design SQUID magnetometer at temperatures between 5 K and 300 K.

3. Results and discussion

The combustion synthetic routes are difficult to control and can cause a highly non-uniform temperature profile on the sample. In the liquid mixing technique Pechini-type method [40], the process chemistry can be controlled, viscosity, polymer molecular weight of the solution can be tailored by varying the CA/EG ratio and the synthesis temperature so that an uniform solution can be produced. By controlling the temperature of heating the mixture (and implicitly the polyesterification and the formation of large metal/organic polymers) autocombustion with flame can be avoided. In our case, the material did not experience spontaneous combustion, after judicious thermal treatment. The ash of the gel after charring at 400 °C in the mantle heater, or "precursor" material, shows an amorphous character. The amorphous precursor is made of soft black shiny particles, Fig. 1A shows SEM micrographs revealing the typical macro-sized precursor particles at different magnification. Some particle surfaces reveal the disgregation of the big particles in smaller micron-sized particles (Fig. 1B).

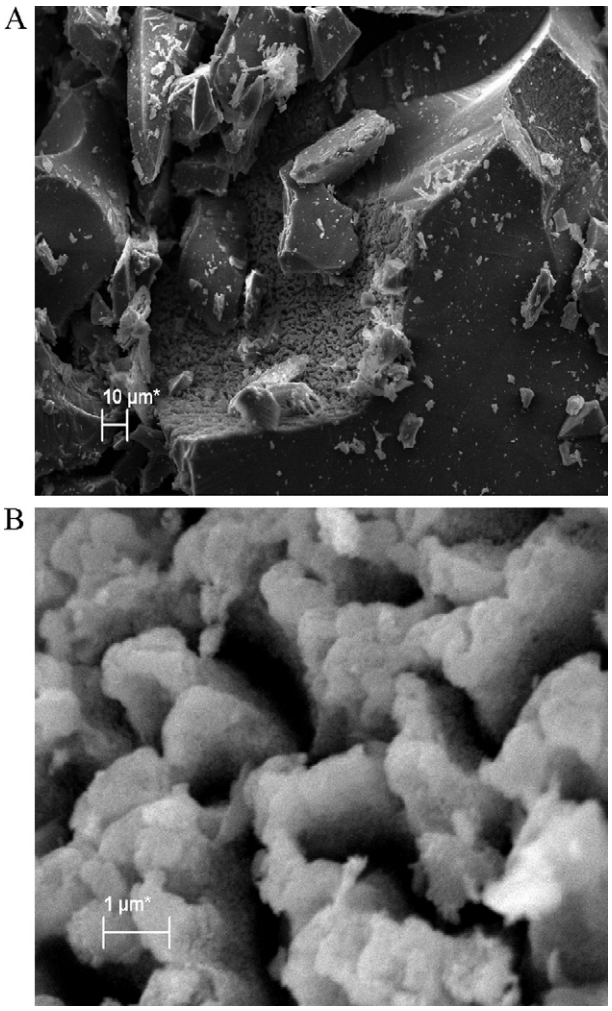

Fig. 1. (A and B) SEM micrographs of the $LaFeO_3$ amorphous precursor.

The combustion of the organic part of the amorphous precursor between 300 °C and 500 °C is a strongly exothermic process associated to the evolution of large amounts of gas resulting in major weight loss. The evolution of the gas not only helps the precursor material to disintegrate but also to dissipate the heat of decomposition, thus inhibiting agglomeration and sintering of the fine particles and helping the instantaneous formation of perovskite oxides. During charring, spontaneous combustion can occur easily raising the sample temperature and determining undesirable product crystallization. The temperature of heat treatment influences the reactivity and particle size. The thermal evolution of the precursor as crystallization, crystal size, presence of agglomerates and the formation of polycrystalline particles was followed in detail.

Thermal treatment at 500 °C results in the break-up of the macrosized amorphous precursor into hard smaller particles. The powder became lighter in colour from black to dark brown to almost brown-orange, the dark colour revealing the carbon presence in the material from the combustion process. At this temperature the La–Fe precursor has lost all its organic part; SEM micrographs of the hard particles result of the break up of the amorphous precursor macro-sized particles (Fig. 2A and B) reveals that they are in fact agglomerates of nanocrystalline seeds, clearly observed at higher magnification images of the particles surface

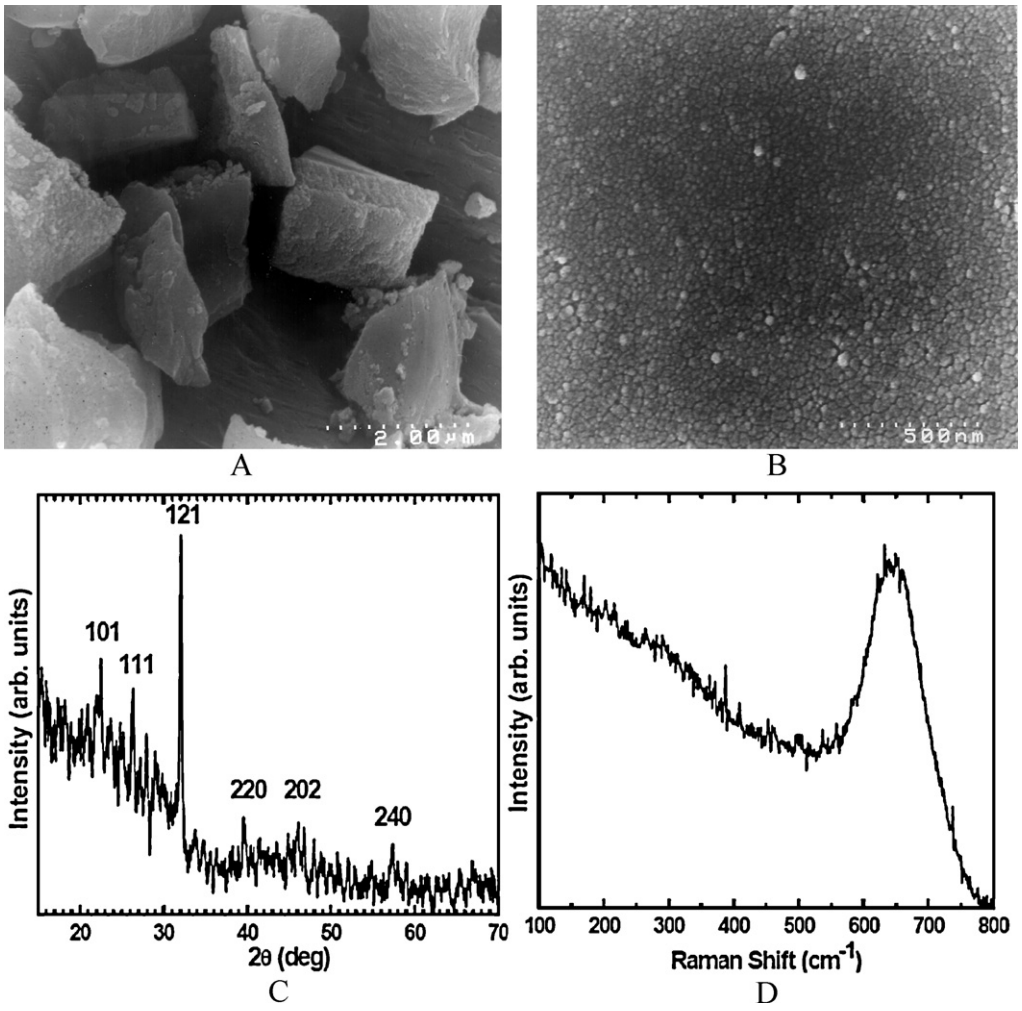

Fig. 2. $LaFeO_3$ powder after the precursor was treated at 500 °C: (A and B) SEM micrographs; (C) XRD pattern; (D) Raman spectrum.

(Fig. 2B). Crystallization of $LaFeO_3$ with orthorhombic symmetry takes place already at temperature as low as 500 °C. The XRD pattern after the precursor was treated at 500 °C (Fig. 2C) shows the main features attributed to perovskite $LaFeO_3$ crystallites as well as a prominent wide bump from the amorphous part contribution to the spectra. Raman measurements were carried out as a sensitive tool to study the crystallization process from amorphous and to determine the optimum conditions for thermal treatment at early stage crystallization. Raman vibrational spectroscopy is known to be a powerful technique to determine the structure distortion and oxygen motion of perovskite-type materials and study order–disorder effects in the lattice at different temperatures [38,41–43]. The Raman spectrum in Fig. 2D shows a single wide band around 650 cm^{-1}, indicating a highly disordered anion lattice of the $LaFeO_3$ nanocrystallites.

Our structural observations based on SEM, XRD and Raman measurements demonstrate that at temperatures above the onset of crystallization a carbon rich amorphous phase still remains, holding together the nanocrystallites in hard agglomerates of nanosized crystallites and the material is in fact an inorganic composite of both amorphous and crystalline phases.

The XRD pattern, Raman spectrum and SEM image of the samples calcined at 550 °C are shown in Fig. 3A–C. The SEM micrograph (Fig. 3A) reveals the formation of disperse particles with homogeneous diameters in the range 30–50 nm. A mean particle size of ~40 nm was calculated from over 200 $LaFeO_3$ nanocrystals in SEM micrographs. The XRD pattern (Fig. 3B) is characteristic of the monophase perovskite according to the JCPDS File 37-1493. This XRD pattern confirms that the lowest calcination temperature to obtain pure phase perovskite LF nanocrystallites is 550 °C; crystallization of the amorphous part is complete at this temperature.

Amorphous carbon is a common impurity formed during the combustion of the organic part in samples prepared by polymerizable complex method and it is not normally detected by XRD, but is readily detected by Raman spectroscopy. The Raman spectrum (Fig. 3C) clearly shows the absence of the D and G bands (~1350 cm^{-1} and ~1480 cm^{-1}, respectively) of amorphous carbon in the higher Raman shift region of Fig. 3C, demonstrating that solid carbon is not present in the sample treated at 550 °C. The structural observations confirm the formation of single phase $LaFeO_3$ nanocrystalline powders of 30–50 nm particle size.

The structure of the nanocrystallites were further analyzed in higher detail. Fig. 4 shows the TEM micrographs and ED pattern of the sample treated at 550 °C clearly displaying the obtained nanocrystallites and the characteristic polycrystalline rings of $LaFeO_3$ in the ED pattern. Based on TEM/ED measurements, we have

Table 1
Proportion of amorphous phase after each calcination temperature.

Temperature (°C)	Amorphous (vol%)
400	>90
500	~20
550	–

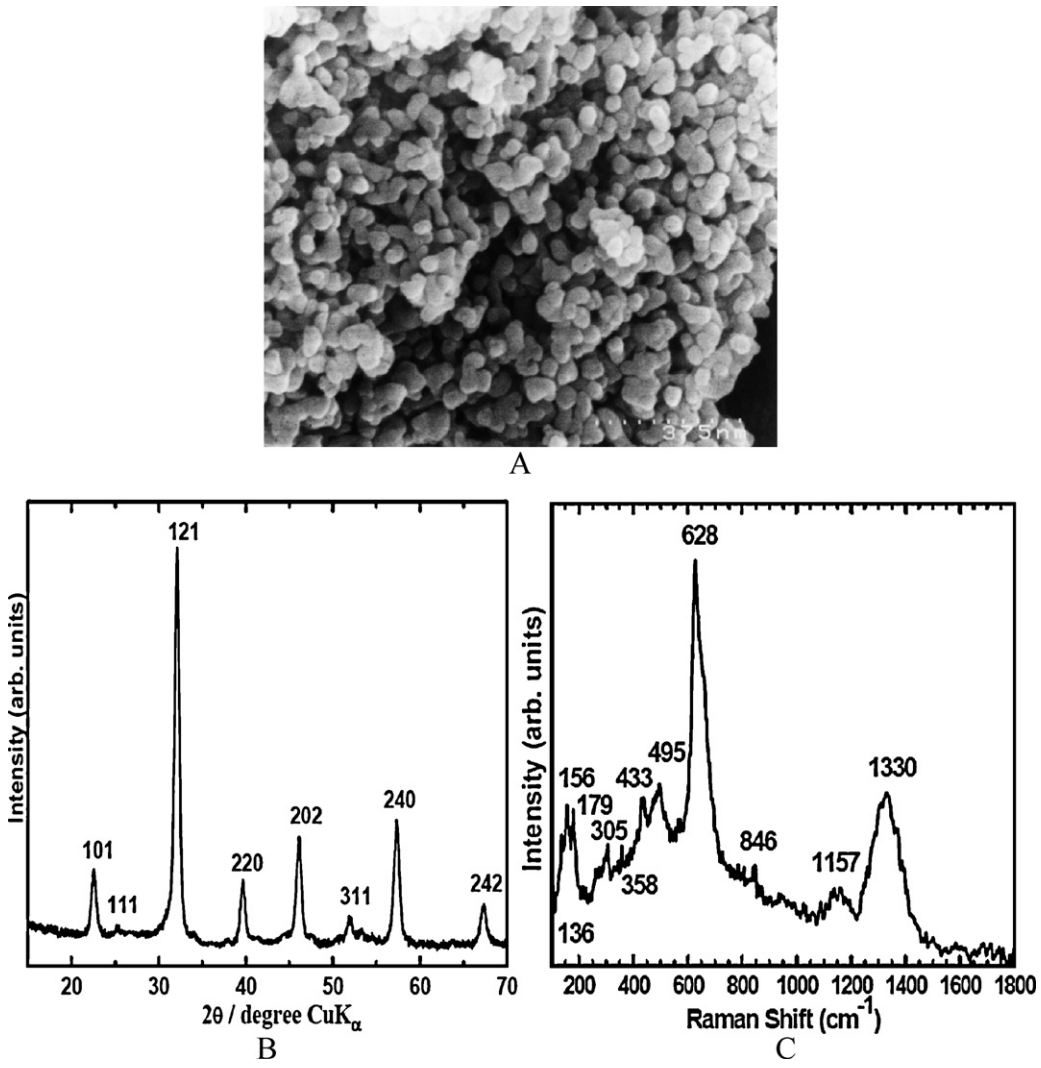

Fig. 3. $LaFeO_3$ nanocrystallites obtained after the precursor was treated at 550 °C: (A) SEM micrograph of the nanocrystalline powder; (B) XRD pattern; (C) Raman spectrum.

estimated the proportion of amorphous phase after each calcination temperature, 400, 500 and 550 °C, and the results are shown in Table 1.

Fig. 5A and B shows the $LaFeO_3$ nanocrystallites obtained at temperatures of 650 °C and 900 °C, the highest temperature used for thermal treatment. Rounded shape, homogeneous, uniform grain size nanoparticles with average size of 55 nm are observed in the powder treated at 650 °C (Fig. 5A). An interesting aspect to take into consideration is that no significant growth of particles was noticed with the increase of the temperature to 650 °C; the particle size remained almost constant between 500 °C and 650 °C. The average crystal size increased, from 30–50 nm to 100–120 nm, at temperatures between 700 °C and 900 °C, results observed both in SEM (Fig. 5B) and TEM (Fig. 6). Fig. 6 illustrates TEM micrographs of $LaFeO_3$ nanoparticles treated at 700 °C showing the development of grain boundaries in sintered chain-like nanoparticle aggregates. Transmission electron microscopy revealed that $LaFeO_3$ was composed of fine particles linked together; bright field and dark field images indicated that the linked particles were individual crystals with no indication of an intercrystalline amorphous phase at grain boundaries. Increasing temperature to 900 °C determined the further increase in nanocrystallite size and formation of grain boundaries and sintering. Sinterization of the powder, bounding of the grains and grain growth are observed at this temperature. Local sinterization occurred at 900 °C without excess of grain growth, which proves the high reactivity of the ceramic powders synthesized by the polymerizable complex method and indicates that finely grained $LaFeO_3$ ceramics could be obtained by sintering the obtained powders at temperatures below 1000 °C.

TEM and HRTEM were employed to obtain information about the structure of the produced $LaFeO_3$ aggregates at 900 °C (Fig. 7) and showed crystallite particles with an average size around 100 nm, or higher in the case of larger crystals result of the local sintering of several nanocrystallites, consistent with average crystalline sizes calculated from the peak broadening in X-ray diffraction using the Debye–Scherrer method and with the average particle size obtained from SEM images (Fig. 5). Concordance between the grain size from SEM and TEM measurements and XRD crystalline domain size indicates that the observed $LaFeO_3$ nanoparticles crystallized directly from the amorphous phase as single domain crystallites. The $LaFeO_3$ nanocrystallites develop a grain boundary network structure, illustrated in Fig. 7A and B, revealing local sintering and the formation of grain boundaries; dislocation networks are clearly seen associated with the grain boundaries in the TEM micrographs. HRTEM measurements demonstrated a random orientation of the crystallites and a good crystalline order inside the orthoferrite particles. The nanoparticles exhibit clearly resolved lattice fringes with the interplanar spacing of 0.39 nm and 0.28 nm, assigned to the (1 0 1) plane and (1 2 1) plane respectively, of the orthorhombic $LaFeO_3$ structure indicating

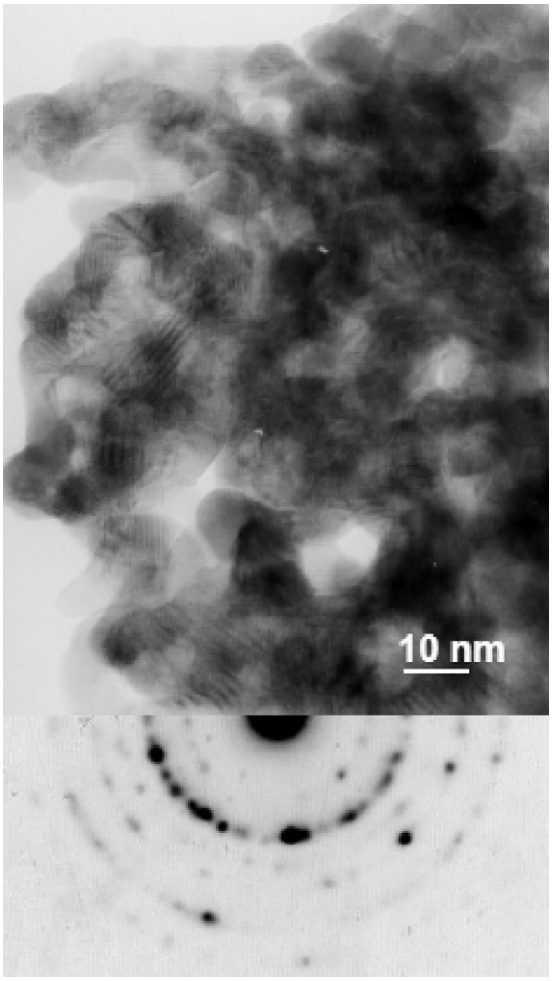

Fig. 4. TEM micrograph and ED pattern of the precursor calcined at 550 °C.

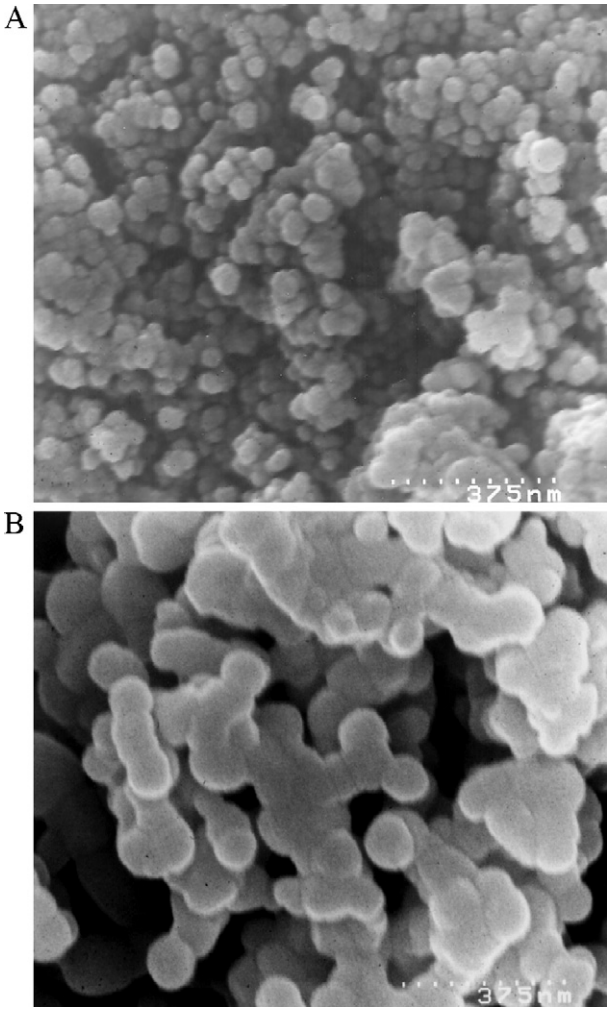

Fig. 5. SEM micrographs of the $LaFeO_3$ nanocrystallites treated at (A) 650 °C; (B) 900 °C.

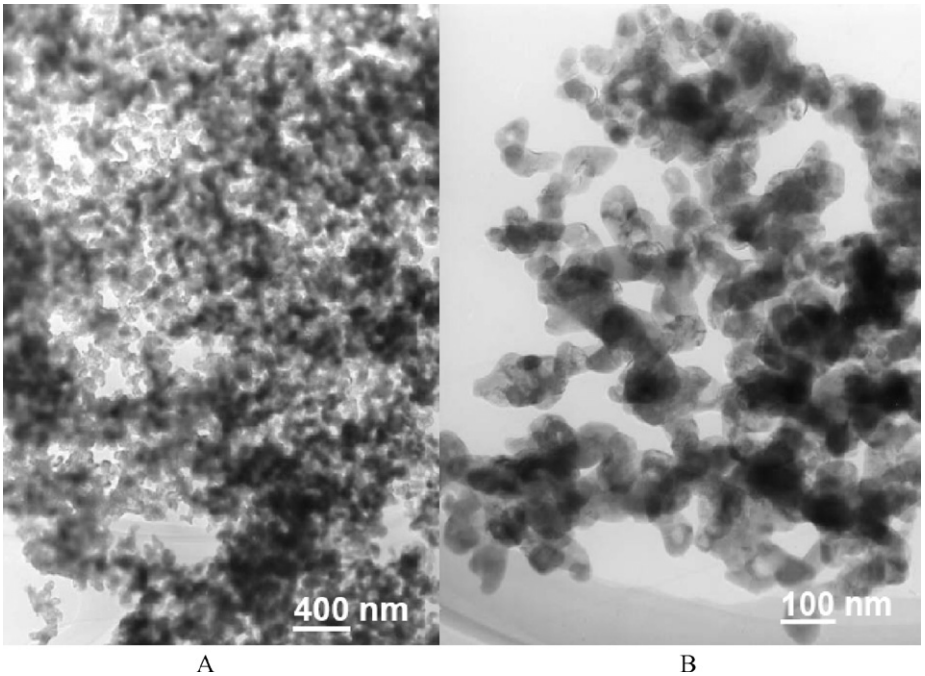

Fig. 6. (A and B) TEM micrographs of the nanocrystalline grains of $LaFeO_3$ formed from the precursor at 700 °C.

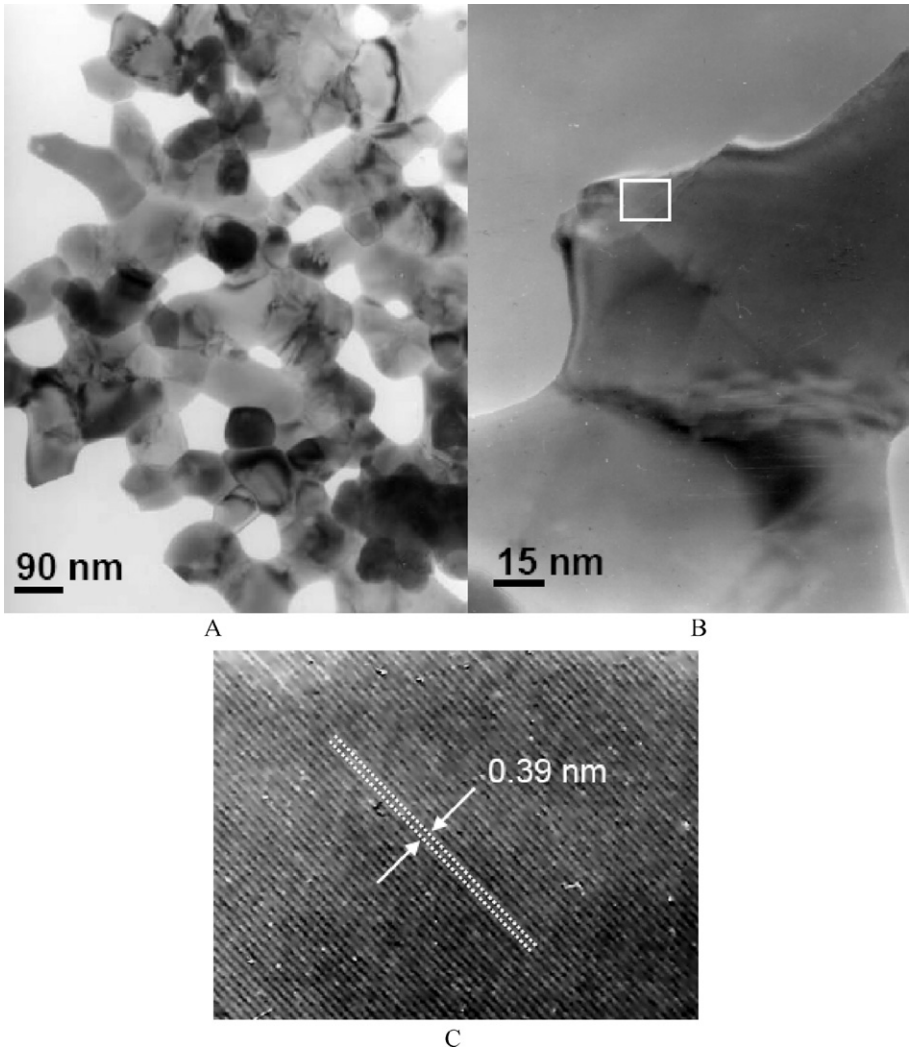

Fig. 7. (A and B) TEM images of the formation of grain boundaries and grain boundaries networks during partial sintering of the $LaFeO_3$ nanocrystals at 900 °C; (C) HRTEM lattice image of the region marked with a square in Fig. 7B.

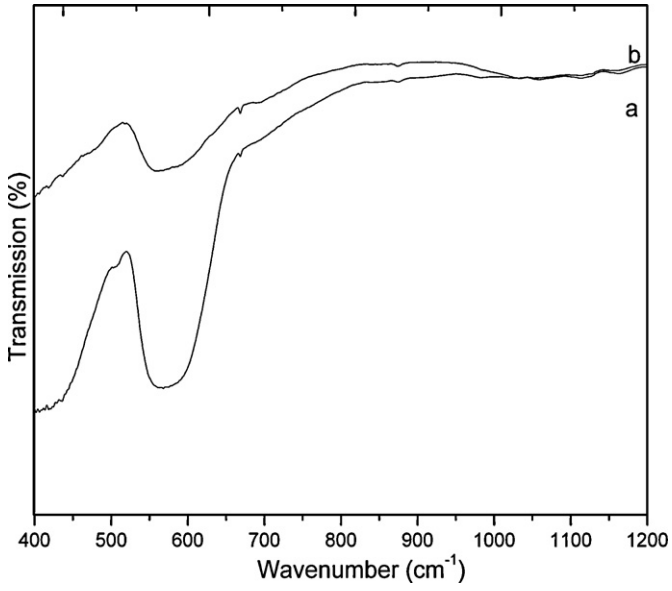

Fig. 8. FT-IR spectra of $LaFeO_3$ powders treated at: (A) 700 °C; (B) 900 °C.

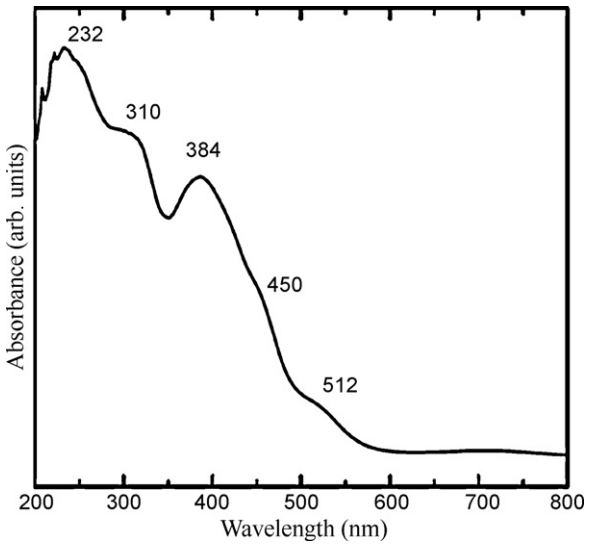

Fig. 9. The UV–vis spectroscopy results for the powders of $LaFeO_3$ treated at 700 °C.

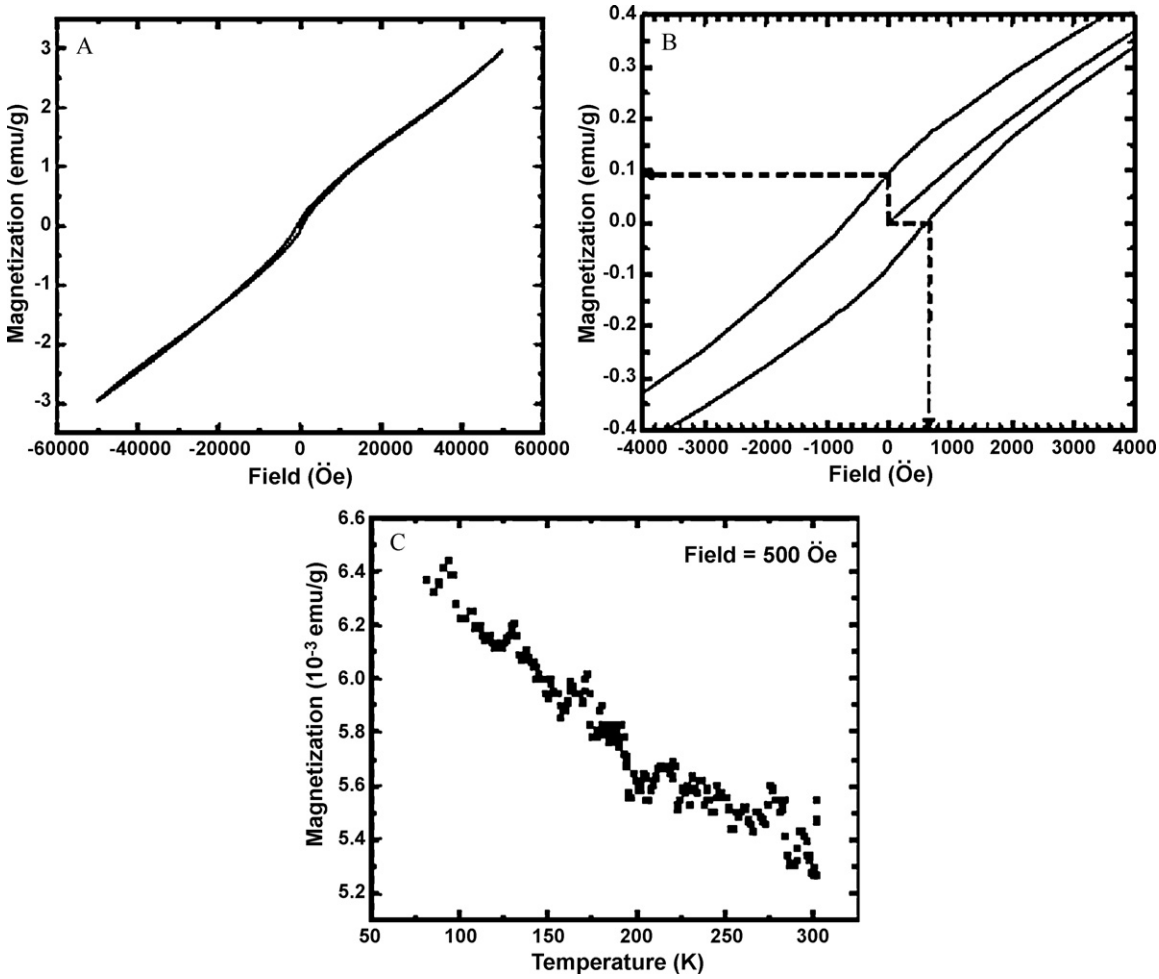

Fig. 10. (A) Magnetization curve at 5 K of $LaFeO_3$ calcined at 900 °C; (B) enlarged views of the hysteresis loop in the low-field region; (C) temperature dependence of the magnetization at an applied field of 500 Öe.

the formation of high quality orthorhombic $LaFeO_3$ nanocrystals, in agreement with the XRD pattern (Fig. 7C). Fig. 7C shows the detailed lattice image of the crystallite in Fig. 7B.

The formation of lanthanum orthoferrite was studied also by IR spectroscopy analysis which indicated the characteristic vibrational bands of the oxide. The FT-IR spectra of $LaFeO_3$ powders treated at 700 °C and 900 °C are shown in Fig. 8. The spectra showed bands in the higher wavenumber region of 650–500 and 450–370 cm^{-1} arising from the stretching modes and deformation modes of the FeO_6 octahedra, respectively [44,45]. Pure rare earth ferrites have no bands in the region 4000–1000 cm^{-1} and the characteristic bands appear only between 600 cm^{-1} and 250 cm^{-1} indicating the absence of any impurity. Our spectra display bands at 383, 400, 420, 450, 558, 623 cm^{-1} and agree with those reported in the literature for $LaFeO_3$ [44–55]. The spectra present an intense band at 558 cm^{-1} with a shoulder at 623 cm^{-1}.The frequency band at 558 cm^{-1} was assigned to the Fe–O asymmetric stretching vibration mode which involves internal motion of a change in Fe–O bond length, whereas the shoulder can be assigned to the symmetric stretching vibration of Fe–O–Fe bands of the BO_6 octahedra [46,47]. All the ferrites show a single band around 400 cm^{-1} [44]. The bands at lower frequencies correspond to the bending mode sensitive to changes in Fe–O–Fe bond angle. Bands associated to La(III)–O stretching motion can also appear in this region [46,47]; in the spectra of the sample treated at 900 °C a weak band appeared at 721 cm^{-1} which may be attributed also to La–O bond. The complex spectra allow the observation of well defined absorption bands typical of ABO_3 perovskites and agree well with the reported spectra in the literature [46–56].

UV–vis spectroscopy has been used to characterize the optical properties of the LF nanoparticles. Once the LF phase formed at 500 °C, UV–vis spectroscopy results were the same for all thermal treatment temperatures. Above this temperature the powders treated at different temperatures kept the same colour. Fig. 9 shows the results for the powders of $LaFeO_3$ treated at 700 °C. The absorption bands shown are observed at 512, 450, 384, 310, 232 nm, but the spectrum reveals a main absorption broad band at 384 nm. This main band may be attributed to the band gap electronic transition from the valence band to conduction band O_{2p}–Fe_{3d} and the spectrum allows us to estimate the optical band gap E_g to be 3.23 eV, displaced to a higher wavenumber compared to the reported one by Wang and Farhadi [22,56]. The bands corresponds essentially Fe^{3+} species as expected for d–d and ligand to metal charge transfer absorption bands of Fe^{3+} in octahedral coordination [57,58].

3.1. Magnetic properties of nanocrystalline $LaFeO_3$

The remarkable magnetic properties of the rare earth orthoferrite family of crystals ($REFeO_3$) have attracted continued experimental and theoretical interests. The direct magnetic interaction between nearest neighbors Fe^{3+} moments in this case is negligible. Instead, the spins are coupled through the oxygen ions by the mechanism of super exchange interaction. This interaction is predominantly antiferromagnetic; however, it has an antisym-

metric component that causes a slight canting of the moments of adjacent iron atoms and a resultant weak ferromagnetic moment as well. Magnetic measurements were performed on the nanocrystalline $LaFeO_3$ powder. The magnetization vs. magnetic field curve $M(H)$ at 5 K for $LaFeO_3$ calcined at 900 °C, shown in Fig. 10A and B, reveals a hysteresis loop with a spontaneous magnetization. The coercive field (H_c) is 600 Öe and the spontaneous magnetization is about 0.10 emu/g. The maximum field applied, 50 kÖe does not saturate the magnetization, and the maximum magnetization at this applied field is 3.0 emu/g. The shape of the hysteresis loop is characteristic of weak ferromagnetism, and the non-saturation of the magnetization is characteristic of antiferromagnetic ordering of the spins in the nanoparticles. The temperature dependence of magnetization behavior at a magnetic field of 500 Öe, of the sample calcined at 900 °C, is also presented in Fig. 10C. The magnetization increases with the decrease of temperature, which reveals that the system is mainly dominated by the weak ferromagnetism (WFM), due to the small crystallite size. Normally, the $LaFeO_3$ system is either weakly ferromagnetic (WFM) or antiferromagnetic (AFM) with a Néel temperature above 300 K [59]. For a 30 nm $LaFeO_3$ particle size system, different authors observed WFM, Qi et al. [60] reported a coercive field of ~90 Öe and a saturation magnetization M_s of ~2.75 emu/g at room temperature and Shen et al. [61] reported a coercive field of 137 Öe and a spontaneous magnetization about 0.10 emu/g, while Sivakumar et al. [62] reported values of ~250 Öe and ~0.04 emu/g, attributed to the increase in the magneto-crystalline anisotropy with the decrease in particle size in nanosized crystallites. Qi et al. [60] observed that the AFM interaction becomes dominant when $LaFeO_3$ nanocrystallites obtained by the sol–gel autocombustion method are calcined, while WFM is observed for non-calcined $LaFeO_3$ powder. As La^{3+} is non-magnetic, the magnetic interaction between La^{3+} and Fe^{3+} is absent. The magnetic super-exchange interactions between the Fe ions result in collinear AFM spin order which contributes to the AFM coupling along a particular crystallographic direction. However, low symmetry of the distorted orthorhombic perovskite-type structure leads to the tilt of FeO_6 octahedra. Consequently, a canted spin order is also formed in the Fe lattice, which gives rise to WFM along another crystallographic direction [59–62]. Therefore, both AFM and WFM ordering can be observed in the system, also influenced by the particle size and morphology.

4. Conclusions

The polymerizable complex method offers low crystallization temperature of single phase ferromagnetic $LaFeO_3$ nanopowder with a homogeneous microstructure. The carbon content in the precursor is completely eliminated by thermal treatment at 550 °C, without the formation of agglomerates or inhomogeneities in grain size as the result of partial sintering. Nanopowders of $LaFeO_3$ with crystal size of 30–50 nm were obtained at temperatures as low as 550 °C, without organic or carbon contamination. High-resolution electron microscopy measurements reveal that the nanopowder is composed of single crystalline grains at 550 °C. Dislocations networks and other domain boundary-related features are clearly observed after treatments at 700 and 900 °C of the highly sinterable nanopowder. Formation of grain boundaries, sintering and grain growth begins at about 700 °C. The average particle size reaches 100–120 nm after successive thermal treatments at 650, 700 and 900 °C. The magnetization vs. magnetic field curve $M(H)$ at 5 K for $LaFeO_3$ calcined at the highest temperature of 900 °C showed weak ferromagnetism and the non-saturation of the magnetization characteristic of antiferromagnetic ordering of the spins in the nanoparticles. Both AFM and WFM ordering can be observed in the system, influenced by the particle size and morphology.

The results observed during the thermal evolution of the $LaFeO_3$ precursor can find application in the production of different pure single-phase homogeneous nanopowders of $LaFeO_3$-based ceramics, including $LaM_xFe_{1-x}O_3$ solid solutions with other transition metals (M = Co, Mn) perovskites which are of great interest due to their electronic and magnetic properties.

References

[1] F. Bidrawn, S. Lee, J.M. Vohs, R.J. Gorte, J. Electrochem. Soc. 155 (7) (2008) 660–665.
[2] J.N. Kuhn, U.S. Ozkan, J. Catal. 253 (1) (2008) 200–211.
[3] J.R. Mawdsley, T.R. Krause, Appl. Catal. A: Gen. 334 (1–2) (2008) 311–320.
[4] G. Pecchi, P. Reyes, R. Zamora, L.E. Cadus, J.L.G. Fierro, J. Solid State Chem. 181 (4) (2008) 905–912.
[5] X. Liu, H. Ji, Y. Gu, M. Xu, Mater. Sci. Eng. 133 (1–3) (2006) 98–101.
[6] H.J.M. Bouwmeester, A.J. Burggraaf, Membr. Sci. Technol. 4 (1996) 435–528.
[7] A.L. Shaula, V.V. Kharton, N.P. Vyshatko, E.V. Tsipis, M.V. Patrakeev, F.M.B. Marques, J.R. Frade, J. Eur. Ceram. Soc. 25 (4) (2005) 489–499.
[8] J.W. Seo, E.E. Fullerton, F. Nolting, A. Scholl, J. Fompeyrine, J.-P. Locquet, J. Phys. Condens. Matter. 20 (26) (2008) 1–10.
[9] E.D. Wachsman, in: T. Hirai, S.I. Hirano, Y. Takeda (Eds.), The Ceramic Society of Japan, 1996, pp. 129–143.
[10] J.W. Stevenson, T.R. Armstrong, R.D. Carneim, L.R. Pederson, W.J. Weber, J. Electrochem. Soc. 143 (9) (1996) 2722–2729.
[11] M. Cherry, M.S. Islam, C.R.A. Catlow, J. Solid State Chem. 118 (1) (1995) 125–132.
[12] F. Prihor-Gheorghiu, A. Ianculescu, P. Postolache, N. Lupu, M. Dobromir, D. Luca, L. Mitoseriu, J. Alloys Compd. 506 (2) (2010) 862–867.
[13] M. Popa, L.V. Hong, M. Kakihana, Phys. B: Condens. Matter. 327 (2–4) (2003) 233–236.
[14] L.G. Tejuca, J.L. Fierro, J.M.D. Tascon, Adv. Catal. 36 (1989) 237–328.
[15] M. Popa, S. Preda, D. Crespo, J.M. Calderon Moreno, V. Fruth, J. Am. Ceram. Soc. 90 (2007) 2723–2727.
[16] N.Q. Minh, J. Am. Ceram. Soc. 76 (1993) 563–588.
[17] M. Popa, S. Preda, V. Fruth, K. Sedlackova, C. Balazsi, D. Crespo, J.M. Calderon-Moreno, Thin Solid Films 517 (8) (2009) 2581–2585.
[18] T. Inoue, N. Seki, K. Eguchi, H. Arai, J. Electrochem. Soc. 137 (8) (1990) 2523–2527.
[19] T. Yao, A. Ariyoshi, T. Inui, J. Am. Ceram. Soc. 80 (9) (1997) 2441–2444.
[20] A. Chaudhuri, S. Mitra, M. Mandal, K. Mandal, J. Alloys Compd. 491 (1–2) (2010) 703–706.
[21] A.D. Jadhav, A.B. Gaikwad, V. Samuel, V. Ravi, Mater. Lett. 61 (10) (2007) 2030–2032.
[22] M. Kumar, S. Srikanth, B. Ravikumar, T.C. Alex, S.K. Das, Mat. Chem. Phys. 113 (2–3) (2009) 803–815.
[23] M. Popa, J. Frantti, M. Kakihana, Solid State Ionics 154–155 (2002) 135–141.
[24] Y. Wang, J. Zhu, L. Zhang, X. Yang, L. Lu, X. Wang, Mater. Lett. 60 (13–14) (2006) 1767–1770.
[25] H. Shen, G. Cheng, A. Wu, J. Xu, J. Zhao, Phys. Status Solidi A 206 (7) (2009) 1420–1424.
[26] N. Russo, D. Fino, G. Saracco, V. Specchia, Catal. Today 137 (2–4) (2008) 306–311.
[27] M. Popa, J. Frantti, M. Kakihana, Solid State Ionics 154–155 (2002) 437–445.
[28] J. Shu, S. Kaliaguine, Appl. Catal. B: Environ. 16 (4) (1998) L303–L308.
[29] X.P. Dai, Q. Wu, R.J. Li, C.C. Yu, Z.P. Hao, J. Phys. Chem. B 110 (51) (2006) 25856–25862.
[30] T. Xian, H. Yang, X. Shen, J.L. Jiang, Z.Q. Wei, W.J. Feng, J. Alloys Compd. 480 (2) (2009) 889–892.
[31] X. Qi, J. Zhou, Z. Yue, Z. Gui, L. Li, Ceram. Int. 29 (2003) 347–349.
[32] M. Siemons, A. Leifert, U. Simon, Adv. Funct. Mater. 17 (13) (2007) 2189–2197.
[33] A.E. Giannakas, A.K. Ladavos, P.J. Pomonis, Appl. Catal. B: Environ. 49 (3) (2004) 147–158.
[34] W. Zheng, R. Liu, D. Peng, G. Meng, Mater. Lett. 43 (1–2) (2000) 19–22.
[35] A. Sivakumar, A. Gedanken, W. Zhong, Y.H. Jiang, Y.W. Du, I. Brukental, D. Bhattacharya, Y. Yeshurun, I. Nowik, J. Mat. Chem. 14 (4) (2004) 764–769.
[36] S. Nakayama, M. Sakamoto, K. Matsuki, Y. Okimura, R. Ohsumi, Y. Nakayama, Y. Sadaoka, Chem. Lett. 21 (11) (1992) 2145–2148.
[37] S. Farhadi, N. Rashidi, J. Alloys Compd. 503 (2) (2010) 439–444.
[38] M. Popa, J.A. Calderon-Moreno, J. Eur. Ceram. Soc. 29 (11) (2009) 2281–2287.
[39] J.M. Calderón-Moreno, E. Camargo, Catal. Today 78 (2003) 539.
[40] M. Kakihana, J. Sol–Gel Sci. Technol. 6 (1996) 7–55.
[41] M. Kakihana, Trends Appl. Spectrosc. 1 (1993) 261–311.
[42] J.M. Calderon-Moreno, M. Yoshimura, Solid State Ionics 154–155 (2002) 125–133.
[43] D. Nelis, J.M. Calderon-Moreno, M. Popa, M.K. van Bael, J. Mullens, L.C. van Poucke, J. Eur. Ceram. Soc. 26 (4–5) (2006) 409–415.
[44] V. Subba Rao, C.N.R. Rao, J.R. Ferraro, Appl. Spectrosc. 24 (4) (1970) 436–445.
[45] M.M. Abou-Sekkina, M.M. El-Kersh, O.A. Shalma, J. Radioanal. Nucl. Chem. 241 (1) (1999) 15–24.
[46] M. Couzi, P.V. Huong, Ann. Chim. 9 (1) (1974) 19–29.
[47] A.E. Lavat, E.J. Baran, Vibrat. Spectrosc. 32 (2) (2003) 167–174.
[48] M. Daturi, G. Busca, R.J. Willey, Chem. Mater. 7 (11) (1995) 2115–2126.
[49] M. Couzi, P.J. van Huong, J. Chim. Phys. (1972) 1339–1347.
[50] P. Ganguly, N.Y. Vasanthacharya, J. Solid State Chem. 61 (2) (1986) 164–170.

[51] P.V. Gosavi, R.B. Biniwale, Mater. Chem. Phys. 119 (1–2) (2010) 324–329.
[52] S. Tajima, A. Masaki, S. Uchida, T. Matsuura, K. Fueki, S. Sugai, J. Phys. C 20 (23) (1987) 3469–3484.
[53] M. Bellakki, B.J. Kelly, V. Manivannan, J. Alloys Compd. 489 (2010) 64–71.
[54] S. Li, L. Jing, W. Fu, L. Yang, B. Xin, H. Fu, Mater. Res. Bull. 42 (2007) 203–212.
[55] B.P. Barbero, J.A. Gamboa, L.E. Cadus, Appl. Cat. B 65 (2006) 21–30.
[56] S. Farhadi, Z. Momeni, M. Taherimehr, J. Alloys Compd. 471 (1–2) (2009) L5–L8.
[57] A.B.P. Lever, Inorganic Electronic spectroscopy, 2nd ed., Elsevier, New York, 1984, p. 450.
[58] C.K. Jørgensen, Absorption Spectra and Chemical Bonding in Complexes, Pergamon Press, NY, 1962, pp. 292.
[59] B. Ita, P. Murugavel, V. Ponnambalam, A.R. Raju, Proc. Indian Acad. Sci. (Chem. Sci.) 115 (5–6) (2003) 519–524.
[60] X.W. Qi, J. Zhou, Z.X. Yue, Mater. Chem. Phys. 78 (1) (2003) 25–29.
[61] H. Shen, G.F. Cheng, A.H. Wu, Phys. Status Solidi A 206 (7) (2009) 1420–1424.
[62] A. Sivakumar, A. Gedanken, W. Zhong, J. Mater. Chem. 14 (4) (2004) 764–769.